Microengineering 3D Collagen Matrices with Tumor-Mimetic Gradients in Fiber Alignment

*Indranil M. Joshi, Mehran Mansouri, Adeel Ahmed, Dinindu De Silva, Richard A. Simon, Poorya Esmaili, Danielle E. Desa, Tresa M. Elias, Edward B. Brown III, and Vinay V. Abhyankar**

Collagen fibers in the 3D tumor microenvironment (TME) exhibit complex alignment landscapes that are critical in directing cell migration through a process called contact guidance. Previous in vitro work studying this phenomenon has focused on quantifying cell responses in uniformly aligned environments. However, the TME also features short-range gradients in fiber alignment that result from cell-induced traction forces. Although the influence of graded biophysical taxis cues is well established, cell responses to physiological alignment gradients remain largely unexplored. In this work, fiber alignment gradients in biopsy samples are characterized and recreated using a new microfluidic biofabrication technique to achieve tunable sub-millimeter to millimeter scale gradients. This study represents the first successful engineering of continuous alignment gradients in soft, natural biomaterials. Migration experiments on graded alignment show that human umbilical vein endothelial cells (HUVECs) exhibit increased directionality, persistence, and speed compared to uniform and unaligned fiber architectures. Similarly, patterned MDA-MB-231 breast cancer cell aggregates exhibit biased migration toward increasing fiber alignment, suggesting a role for alignment gradients as a taxis cue. This user-friendly approach, requiring no specialized equipment, is anticipated to offer new insights into the biophysical cues that cells interpret as they traverse the extracellular matrix (ECM), with broad applicability in healthy and diseased tissue environments.

1. Introduction

Type I collagen fibers are crucial in coordinating cellular activities in native tissues, with aligned fiber domains extending over sub-millimeter to millimeter length scales.[1–3] At the millimeter scale, fiber alignment maintains the organization of cardiac, skeletal, and smooth muscle cells and enables directional force generation along the axis of alignment.[4–6] At the sub-millimeter length scale, aligned fibers guide epithelial, endothelial, and immune cells during tumor invasion,[7,8] angiogenesis,[9,10] and immune trafficking processes,[11] respectively. Here, the aligned fibers provide biophysical contact guidance cues that help cells navigate toward or away from vascular and lymph vessels during the matrix invasion phase of the metastatic cascade. Indeed, in biopsy samples of breast,[7] ovarian,[12] and pancreatic cancer,[8] collagen fibers oriented perpendicular to the tumor interface are a clinical predictor of metastases and poor patient outcomes. Over the past decade, the biological significance of fiber alignment has led to the development of in vitro platforms to study the impact of extracellular matrix (ECM) architecture on cell behavior in healthy and diseased tissue.[13,14]

The overarching goal of 3D in vitro model systems is to improve the physiological relevance of experiments by replicating tissue-specific environmental cues and matrix architectures. To this end, collagen is a popular biofabrication material because it is the most abundant structural protein in the body and can create hydrogel scaffolds with defined fiber alignment landscapes in the laboratory. As reviewed by several groups, collagen fibers can be aligned using bioprinting approaches,[15,16] electrospinning,[17,18] or by applying external magnetic,[19] electric, strain,[20,21] and flow fields.[22,23] Alternatively, collagen fibers can be reorganized and aligned using embedded, contractile cells followed by decellularization to produce a hydrogel with uniform fiber alignment.[14,24,25] Although these methods effectively create collagen-based hydrogels with homogeneous, millimeter-scale fiber alignment, they cannot replicate the more complex sub-millimeter scale alignment found in vivo.

I. M. Joshi, M. Mansouri, A. Ahmed, D. De Silva, R. A. Simon, P. Esmaili, V. V. Abhyankar
Department of Biomedical Engineering
Rochester Institute of Technology
Rochester, NY 14623, United States
E-mail: vvabme@rit.edu

D. E. Desa, T. M. Elias, E. B. Brown III
Department of Biomedical Engineering
University of Rochester
Rochester, NY 14627, United States

The ORCID identification number(s) for the author(s) of this article can be found under https://doi.org/10.1002/adfm.202308071

DOI: 10.1002/adfm.202308071

The ECM can exhibit sub-millimeter spatial heterogeneity because the matrix architecture is actively reorganized in response to cell-induced traction forces.[26] These cell-substrate interactions introduce local gradients in matrix properties that are sensed and interpreted by resident cells. For example, the motility of epithelial, endothelial, and immune cells in response to graded biophysical “taxis” cues, including stiffness (durotaxis),[27,28] topography (topotaxis),[29,30] tethered biomolecules (haptotaxis),[31] have been extensively studied. Importantly, there is evidence that cells respond to spatially graded cues differently than homogeneous signals.[32–34] This phenomenon is particularly relevant to the tumor microenvironment (TME), where cell-matrix interactions can introduce sub-millimeter fiber alignment landscapes that decay with distance away from the interface (i.e., fiber alignment gradients).[35] However, studies that explore the role of contact guidance in natural materials are primarily limited to collagen or fibrin hydrogels with uniformly aligned fiber architectures.[14,36] Thus, the importance of graded biophysical cues is well-recognized, but fiber alignment gradients have not been widely investigated as a potential guidance cue, likely because an experimentally tractable method to engineer complex alignment gradients in natural materials was not available.

To help develop increasingly biologically relevant in vitro models, we present a geometry-based approach using a constricting and expanding channel design to engineer 3D collagen gels with continuous, graded fiber alignment spanning sub-millimeter to millimeter length scales that can be tuned simply by adjusting the input flow rate. We also describe a flexible experimental approach that enables single cells and cell aggregates to be patterned at defined locations on the alignment gradient to uniquely study migration responses. As a proof of concept, we show that single human umbilical vein endothelial cells (HUVECs) migrate with increased directionality, speed, and persistence on gradient gels compared to uniformly aligned and unaligned gels. We also show that gradients in local alignment strongly bias the directional migration of patterned MDA-MB-231 cell aggregates toward increasing alignment. In contrast, cell aggregates on uniformly aligned gels exhibited bi-directional migration along the fibers and those on unaligned gels displayed random walk behavior. We anticipate that our experimental platform will enable new studies that explore how fiber architectures influence contact guidance in different tissue contexts.

2. Results and Discussion

2.1. SHG Imaging of Biopsy Samples Reveals Sub-Millimeter Gradients in Fiber Alignment

Over the past two decades, it has been established that cells can migrate along aligned collagen fibers within the tumor microenvironment (TME) in a process called contact guidance.[37,38] To study these responses under controlled laboratory conditions, several teams have developed methods to create uniformly aligned 3D collagen gels and quantify migration metrics, including speed and directionality.[36,39] However, intravital imaging studies have revealed that tissue microenvironments contain local spatial variations (gradations) in alignment rather than a homogeneous alignment landscape.[40] Therefore, to build physiologically representative contact guidance features, our first objective was to use second harmonic generation (SHG) imaging to quantify the degree of heterogeneity in banked, de-identified triple negative breast cancer (TNBC) biopsy samples. **Figure 1A** shows a representative SHG image of the tumor stroma, highlighting the variation in alignment observed across the 600 µm section. To assess the degree of fiber alignment present in the TME, the image was divided into three equal regions, and the coefficient of alignment (CoA) was calculated for each region. Figure 1B shows that average CoA values ranged from 0.67 ± 0.04 to 0.34 ± 0.07 across the section (slope = 0.02 CoA units10 µm), with statistically significant differences observed between each section ($n = 7$ samples).

These findings were significant because spatially graded biochemical and biophysical signals present different levels of stimuli across the length of the cell and are known to play an essential role in cell migration.[41–45] These graded cues lead to differential engagement of the signal transduction machinery, resulting in asymmetric force generation in the cytoskeleton that promotes directional migration.[32] Hence, the presence of subtle sub-millimeter scale gradients in the biopsy samples prompted us to ask whether alignment gradients could serve as a signal that promoted directional migration.

While alignment gradients resembling the interface between tendon and bone have been achieved using hard synthetic materials like polycaprolactone and poly(lactic-co-glycolic acid) through electrospinning, creating fiber alignment gradients in soft collagen-based biomaterials remains a challenge.[46–48] Cell-mediated traction forces can be used to locally rearrange fiber architecture (see Figure S1, Supporting Information); however, the resulting gradient characteristics, including slope and range, are challenging to control and reproduce. To the best of our knowledge, no existing technologies are capable of microengineering tunable and reproducible alignment gradients in soft collagen biomaterials. Developing a platform with robust biofabrication capabilities is essential to investigate the role of alignment gradients as a guidance cue in the TME and other tissue microenvironments.

2.2. Fiber Alignment can be Controlled by Introducing Local Extensional Flows in a Microfluidic Channel

To address the need for biofabrication techniques to create physiological fiber alignment gradients, we took inspiration from our previous work, where we used local extensional flows to create 3D collagen hydrogels with uniform fiber.[49] This technique involved injecting a neutralized collagen precursor solution into a channel that featured sequential decreases in width, as shown in **Figure 2A**. At the beginning of each segment, the change in geometry introduced a local increase in velocity along the flow direction (quantified by a positive extensional strain rate, $\dot{\varepsilon}_{xx} = \partial U_x / \partial x$, and labeled in light blue), which transitioned to a constant velocity state within each parallel-walled segment ($\dot{\varepsilon}_{xx} = 0$, labeled in gray). Here, U_x refers to the x component of the velocity vector U, and x is the axial direction. In this design, the collagen precursor solution experienced successively increasing extensional strain rate at the entrance of each segment along the flow direction. We discovered that local extensional flows produced highly aligned fibers in the downstream segments, and

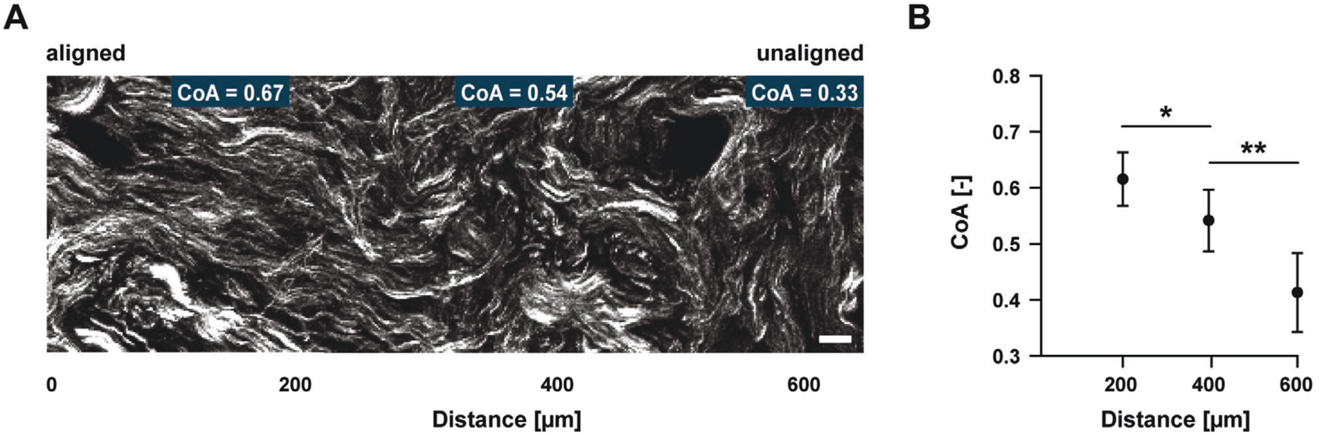

Figure 1. Quantification of fiber alignment gradients in the tumor microenvironment. A) A representative SHG image of tumor collagen from a TNBC patient biopsy sample reveals sub-millimeter gradations in alignment, with CoA ranging from 0.67 to 0.33 across the 600 µm section. Scale bar = 25 µm. B) The CoA is plotted as a function of position along the biopsy sample with statistically significant differences between each section. The data is reported as mean ± standard deviation compared using one-way ANOVA with Tukey's multiple comparisons test. $^{*}p < 0.05$, $^{**}p < 0.002$ ($n = 7$ samples).

the degree of alignment could be controlled as a function of flow rate Figure S3, Supporting Information.[49] The proposed mechanism was consistent with the behavior of other polymer systems and suggested that a pattern of increasing extensional flow in the channel induced directional assembly by promoting electrostatic and hydrophobic interactions in the collagen solution that supported uniformly aligned fiber formation in each segment.[50,51]

Based on these findings, we hypothesized that a channel design that incorporated a combination of positive, zero, and negative extensional flows (i.e., positive and negative values of $\dot{\varepsilon}_{xx}$ along the flow path) could establish a graded fiber alignment architecture, as illustrated schematically in Figure 2B. To confirm that positive (light blue) and negative extensional flows (pink) could be generated within a single channel, we designed a geometry with i) a funnel-like constriction, ii) a constant width region, and iii) an expansion well. As shown in Figure 2C, we used microparticle imaging velocimetry (µPIV) to measure the velocity of the neutralized collagen precursor solution in each region with the input flow rates Q = 500, 100, and 10 µL min^{-1}. As expected, the extensional strain rate was positive ($\dot{\varepsilon}_{xx} > 0$, positive extensional flow) in the constriction, zero in the constant width region ($\dot{\varepsilon}_{xx} = 0$), and negative ($\dot{\varepsilon}_{xx} < 0$, negative extensional flow) upon entering the expansion region. These validation experiments confirmed that the extensional flow patterns the collagen precursor solution experienced along the channel could be controlled as a function of geometry and flow rate.

Next, we tested our hypothesis that a pattern of positive, zero, and negative extensional flows would create continuous gradients in fiber alignment. As shown in **Figure 3**A, neutralized collagen solutions were injected along the path a-a′ at the three flow rates characterized in Figure 2C. After gel formation, the resulting fiber microarchitecture was imaged using confocal reflectance microscopy (CRM). We then plotted CoA as a function of position for all flow rates, with the beginning of expansion defined as x = 0, and positive x values indicating advancing position into the expansion (i.e., toward a′). As shown in Figure 3B,C,

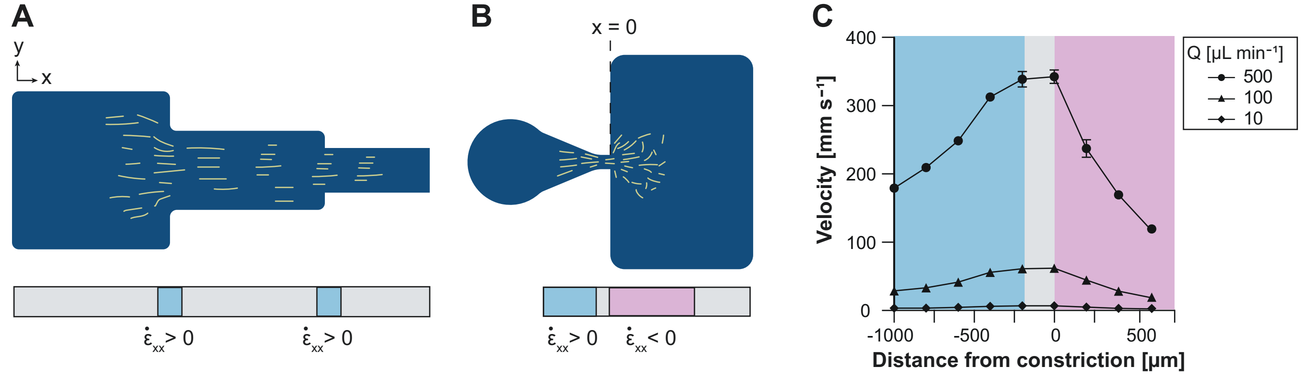

Figure 2. Different extensional flow patterns are introduced by varying the channel geometry. A) A positive and zero extensional flow pattern can be achieved using a sequentially constricting design. Light blue regions indicate areas of transient stretch due to the velocity increase along the flow direction (+x), while grey areas identify regions with constant velocity. B) A pattern of positive (light blue), zero (gray), and negative (pink) extensional flows can be achieved in an expanding and constricting channel design. Self-assembling fibers are shown in yellow. C) µPIV data confirms the expected extensional flow pattern for the geometry shown in panel B at flow rates Q = 500, 100, and 10 µL min^{-1}. Schematics in A and B are not drawn to scale.

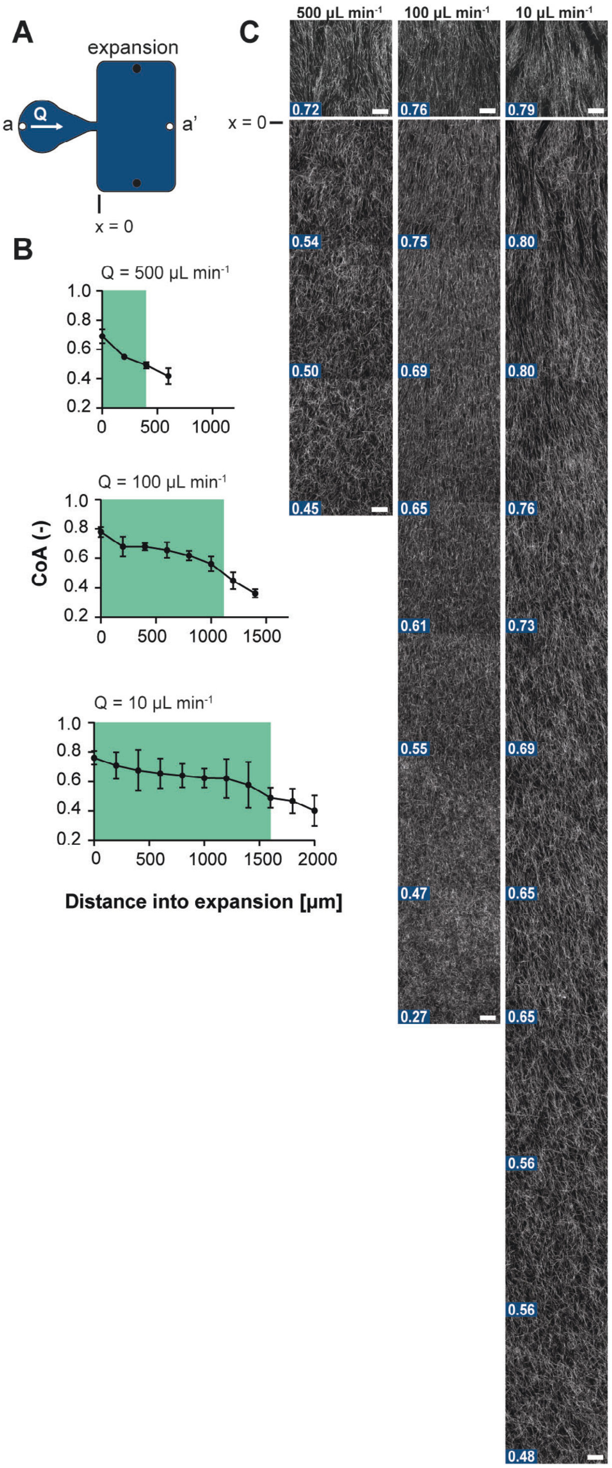

Figure 3. Graded fiber alignment as a function of flow rate. A) A schematic representation of the channel design is shown with the entrance to the expansion well at x = 0 and flow path a-a′. B) The relationship between CoA vs distance into the well is shown for input flow rates Q = 500, 100, and 10 µL min^{-1}, with the entrance to the well defined as x = 0. The shaded green boxes mark the distance into the well over which fibers remain aligned, CoA > 0.5. Data is shown as mean ± SD (*n* = 3 replicates). C) Representative CRM images corresponding to the data in panel B that show continuous alignment gradients after gel formation at each flow rate. CoA values are shown in the bottom left of each image. Scale bar = 25 µm.

fibers were highly aligned (CoA > 0.7) in the parallel-walled region immediately before x = 0 for all flow rates. The fiber alignment decayed continuously in the expansion for all flow rates but with key differences in the slope and the distance over which fibers remained aligned, as indicated by the green-shaded regions. For Q = 500 µL min^{-1}, CoA decreased sharply in the expansion region, transitioning from aligned to unaligned within 500 µm, and created a sub-millimeter scale gradient similar to the TNBC tumor samples. At Q = 100 µL min^{-1}, fiber alignment extended 1.2 mm into the expansion, and at Q = 10 µL min^{-1}, alignment extended 1.5 mm into the expansion region (Figure 3B). Figure 3C shows collagen fibers in the pre-expansion funnel region and montages of the corresponding fiber landscapes for each input flow rate.

Based on these results, we concluded that a pattern of positive, zero, and negative extensional flows in the channel produced defined sub-millimeter to millimeter scale alignment gradients that could be tuned as a function of Q. The mechanism of alignment could be partially explained as follows: in the constricting section, self-assembling collagen subunits were forced into close proximity, stretched, and oriented under the positive extensional flow. As the solution passed into the uniform width region, the velocity was constant (zero extension), and the channel walls constrained the lateral motion of the self-assembling subunits and preserved their orientation. When the collagen solution entered the expansion well, the dramatic increase in the cross-sectional area produced a non-linear decrease in fluid velocity (see Figure 2C). The unconstrained flow in the expansion permitted the oriented subunits to diverge from their upstream positions, followed by diffusive spreading that produced a graded fiber alignment landscape after gel formation.[52,53]

One interesting finding was that the highest input flow rate produced the steepest alignment gradient that transitioned from aligned to unaligned within 500 µm and was similar in scale to the sub-millimeter gradients found in TNBC tumor samples (Figure 1A). In contrast, the slower flow rates exhibited more gradual changes in alignment, with a longer distance over which the fibers remained aligned. One possible explanation for this behavior could be described by considering the Deborah number (De), which is a ratio between the solution relaxation time (λ) and the flow time scale (τ), De = λ/τ. When De > 1, the elastic behavior of the polymer solution dominates, while viscous, liquid-like behavior dominates as De << 0.[54–57] At a flow rate of 500 µL min^{-1}, De = 4.1, suggesting that the elastic response of the collagen solution in the expansion could contribute to the sharp gradient in alignment. Conversely, at the lower flow rates tested (Q = 100 and 10 µL min^{-1}) the response of the solution was dominated by viscous rather than elastic effects (De = 0.74 and 0.08, respectively), producing a gradient with a less pronounced slope. Although the mechanism of gradient formation remains an active area of investigation in our laboratory, the primary goal of this work was to highlight the concept that simple variations in channel geometry could create sub-millimeter to millimeter scale gradients in fiber alignment and provide unique biofabrication capabilities in soft biological materials.

To expand the biomaterial options available with our approach, we also show that our microengineering technique is not limited to collagen gels. We have successfully used collagen/fibronectin, collagen/hyaluronic acid (HA), and glycated collagen to provide

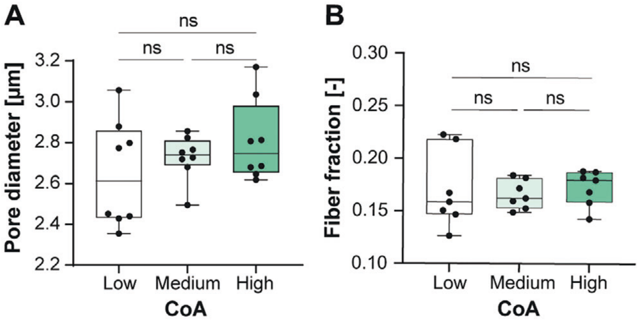

Figure 4. Matrix pore diameter and fiber fraction as a function of CoA. Collagen CRM images were divided into 3 categories, high (green, 0.7 < CoA ≤ 1), medium (light green, 0.5 ≤ CoA ≤ 0.7), and low (white, 0.25 ≤ CoA < 0.5) alignment. A) The box and whisker plots show the pore diameters in the three CoA categories and ANOVA analysis with Tukey's multiple comparison test concluded the values are not statistically different. Box and whisker plots show median, first and third quartiles, and the minimum and maximum values, $n = 7$ independent gels per group. ns = not statistically significant.

a range of options to engineer in vitro models to better represent the architecture and composition of the target tissues (Figure S4, Supporting Information). Our technique is also compatible with photoactivatable methacrylated collagen that allows the matrix modulus to be tuned to match target tissue through exposure to UV light (see Figure S5, Supporting Information). Notably, the collagen microarchitecture was maintained before and after UV exposure, as shown in Figures S6 and S7, Supporting Information. Our approach is also compatible with published methods that control fiber diameter by sequentially varying the gelation temperature from room temperature to 37 °C.[58–60] Thus, our versatile microengineering technique provides a wide range of biomaterial options to achieve in vitro models that faithfully replicate the architecture and composition of natural tissues. We anticipate that this technique can be applied to various fibrous ECM materials, including fibrin and elastin, to further support advancements in soft material biofabrication.

2.3. Matrix Fiber Density and Pore Diameter are not Affected by Collagen CoA

Gradations in matrix pore diameter and fiber density are well-studied taxis cues that guide cell migration through the ECM.[61–63] Thus, after establishing a method to create 3D collagen gels with tunable CoA gradients, we investigated whether CoA influenced pore size and fiber density. We first categorized fiber architecture into three groups: low (0.25 < CoA < 0.5), medium (0.5 ≤ CoA < 0.7), and high (0.7 ≤ CoA < 1). To calculate the pore diameter in each group, we used a standard image processing algorithm to allow for benchmarking against other work.[59] **Figure** 4A shows no statistical differences in pore diameter between the low, medium, and high CoA categories, and the average pore across the groups was 2.72 ± 0.15 µm. Next, we investigated whether CoA influenced fiber density, as measured by the fiber fraction. The relationship between CoA and fiber fraction is shown in Figure 4B, and no statistical differences were found among the three alignment categories, with an average fiber fraction of 0.17 ± 0.02. These values are consistent with those reported in the literature using similar collagen concentrations and gelation conditions.[64,65] Taken together, these analyses provide evidence that fiber alignment can be controlled without influencing bulk pore size or fiber density using our flow-based biofabrication approach.

These findings are relevant because ligand density is directly related to the fiber density in the matrix, and our data show that the fiber density (measured by fiber fraction) is independent of CoA.[59,66] Fiber density and porosity are often used as a proxy for the matrix stiffness.[67–69] Our results indicate that these properties are independent of CoA, suggesting that bulk mechanical properties may not be linked to CoA in our system. We confirmed this finding by measuring the Young's modulus of aligned (CoA = 0.6 ± 0.02) and unaligned (CoA = 0.4 ± 0.02) gels using nanoindentation (See Figure S8, Supporting Information) and found no statistical differences in the stiffness. Taken together, our system could be used to quantify how cell migration is influenced by fiber alignment gradients independent of underlying differences in porosity, density, or mechanical properties that could confound experimental interpretation.

2.4. A Reversibly Sealed Microchannel Allows Direct Access to Microengineered 3D Collagen Gels

After quantifying relationships between CoA, porosity, and fiber density in our gels, we sought to quantify how cells responded to fiber alignment gradients in our microfluidic platform. Microfluidic approaches are well-recognized as experimental tools that enable precise control over the cellular microenvironment.[44,70,71,72] Conventional microfluidic systems are permanently sealed, and the introduction of cells requires that they are included in the self-assembling gel solution or added through ancillary seeding channels.[73–76] Incorporating cells in the gel solution limits the parameter space (e.g., gelation temperature, ionic strength, pH, mechanical strain, or photoinitiator concentration) that can be used to control matrix properties. Incorporating additional seeding channels can complicate designs and introduce sources for bubble formation or clogging that can decrease experimental yield.[77,78] Our microfluidic design simplifies the process of adding cells to the gels by using a bovine serum albumin (BSA) passivated polydimethylsiloxane (PDMS) lid that is sealed reversibly against a through-cut PDMS sheet that contains the desired channel geometry. The completed channel is comprised of a glass coverslip on the bottom, PDMS side walls, and a PDMS lid containing cored access ports. The PDMS lid is peeled off after gel formation, providing full access to the 3D microengineered collagen matrix.[20] We verified that the fiber microarchitecture was not disrupted by comparing fiber alignment before and after the peel off process using CRM. Figure S9, Supporting Information, shows the change in CoA, ΔCoA = 0.02 ± 0.03, with a maximum change of 0.06 CoA units.

Our previous work demonstrates that the open access design allows specialized modules to be attached to the gel layer. These include permeable cell culture membranes, flow modules, and gel deposition modules to support layer-by-layer fabrication.[49] Here, we add cells directly to the gel or use a second PDMS sheet containing a patterning aperture reversibly sealed against the PDMS channel layer to define the location of the added cells.

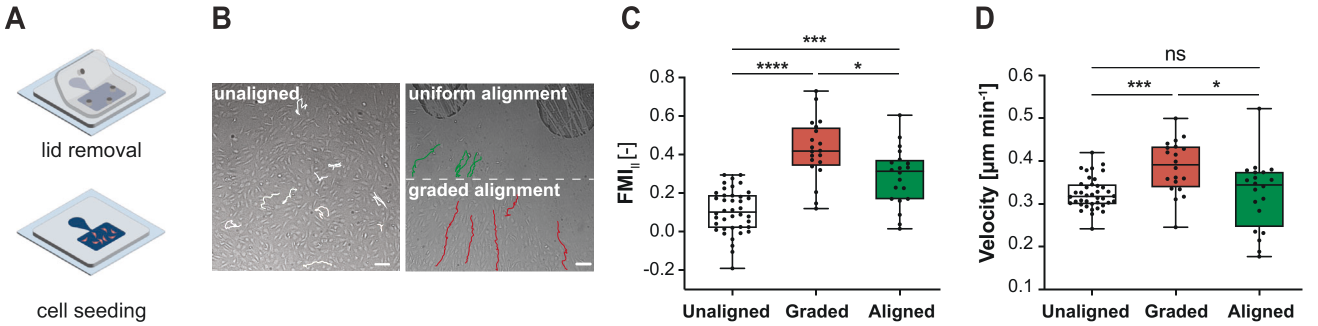

Figure 5. Migration characteristics of HUVECs on unaligned, uniformly aligned, and gradient regions. A) Schematic representation of the PDMS lid to access the engineered hydrogel. Note, the gel is confined to the footprint of channel, and the height is defined by the thickness of the sheet (200 µm). B) Representative migration tracks of ten randomly selected cells on an unaligned gel are shown in white and 5 cells each in gradient region shown in red and uniformly aligned are shown in green. Scale bar = 100 µm. C) The $\text{FMI}_{||}$ of cells on unaligned, uniformly aligned and gradient conditions. Statistical comparison of the data shows cells on the gradient exhibit higher $\text{FMI}_{||}$ than cells on unaligned and uniformly aligned collagen fibers. Data are presented as box and whisker plots show the median, first and third quartiles, minimum and maximum values (*n* = 40 cells on unaligned gel, *n* = 20 cells each for uniformly aligned and gradient regions) compared using one-way ANOVA. D) The migration speed of cells on unaligned, uniformly aligned and gradient are compared. Statistical comparison of the data show cells on gradient exhibit higher migratory speeds than cells on unaligned and aligned collagen fibers, while the cells on aligned and unaligned fibers show no differences in speed. Data presented as box and whisker plot show the median, first and third quartiles, and the minimum and maximum values (*n* = 40 cells on unaligned gel, *n* = 20 cells each for gradient and uniformly aligned region compared using one-way ANOVA. $^{*}p < 0.05$, $^{***}p < 0.0002$, $^{****}p < 0.0001$, ns = not statistically significant).

This cell seeding technique is also compatible with 3D printed or automated dispensing methods. Thus, our approach combines the advantages of conventional microfluidic systems but simplifies the operations typically associated with these approaches.

2.5. HUVECs and MDA-MB-231 Cells Migrate Directionally on Gradient Gels

To begin exploring cell responses on different alignment landscapes, we seeded HUVECs (**Figure 5A**) on a section close to the entrance of the expansion well that contained regions with uniformly aligned (CoA > 0.65) and graded alignment (0.5–0.65), as shown in Figure 5B. Quantifying cell migration in these two regions allowed us to uniquely compare behavior on graded and uniform fiber alignment. We tracked randomly selected cells for 12 h in each region, calculated the Forward Migration Index parallel[79] to the direction of alignment ($\text{FMI}_{||}$), and then quantified the corresponding migration velocity. As shown in Figure 5C, $\text{FMI}_{||}$ in the graded region was statistically larger than in the uniformly aligned region, and the FMI of the unaligned control ($\text{FMI}_{||,\text{ gradient}} = 0.42 \pm 0.1$, $\text{FMI}_{||,\text{ aligned}} = 0.28 \pm 0.1$, and $\text{FMI}_{\text{unaligned}} = 0.1 \pm 0.1$, $p < 0.05$ between groups). The notation for FMI in the unaligned control is described in the methods section. Previous work comparing contact guidance effects between uniformly aligned and unaligned gels reported that directionality increased on the uniformly aligned gels, but velocity did not change.[80] We found similar trends between these groups, but interestingly, the migration velocity on the graded alignment region ($V_{\text{gradient}} = 0.38 \pm 0.06$ µm min^{-1}) was statistically larger than the uniformly aligned region ($V_{\text{aligned}} = 0.32 \pm 0.08$ µm min^{-1}) and unaligned control ($V_{\text{unaligned}} = 0.32 \pm 0.03$ µm min^{-1}).

Next, we fit the migration data in each region to a persistent random walk model[81,82] and found that the relative persistence on the gradient increased by a factor of two compared to the uniformly aligned region and the unaligned controls. The migration video shows that cells on the aligned and gradient regions (Video S1, Video S2, Supporting Information) migrated directionally with limited backward motion, while cells on the unaligned gel exhibited random migration (Video S3 Supporting Information). Taken together, our results showed single cells on alignment gradients exhibited interesting differences in directionality, speed, and persistence. These findings support our premise that graded fiber architectures guide cell responses differently than uniformly aligned conventionally studied in contact guidance.

After showing that single cells responded to graded alignment with enhanced migration behaviors, our next goal was to test whether fiber alignment gradients could bias migration in aggregated cell populations. To do so, we removed the PDMS lid after gradient gel formation and replaced it with a PDMS sheet that contained a circular patterning aperture. An MDA-MB-231 breast cancer cell aggregate was added to the aperture and allowed to settle and attach to the gradient gel. **Figure 6A** shows a representative image with fluorescently labeled MDA-MB-231 cell aggregate positioned within the footprint of the aperture. Cells at the left edge of the aperture experienced a CoA > 0.6, while cells at the right edge experienced a CoA < 0.5. We captured images every 24 h and measured the positions of the left (l_n) and right (r_n) edges of the cell aggregate. We then constructed an enclosed cell envelope encompassing the aggregate shape at each time point. Although this analysis identified a projected area, we confirmed that cells could migrate into the depth of the collagen gel (Video S4, Supporting Information).

To assess the relative migration in each direction, we calculated a biasing metric Ω_n, which compared the ratio of the change in the left edge position (Δl_n) to the difference in the right edge position (Δr_n) between time points. The l_{24} and r_{24} positions were used as the origin to eliminate any initial bias if the aggregate was not centered in the aperture after seeding. As shown in Figure 6B, $\Omega_n > 1$ indicates biased movement toward the left (increasing CoA), $\Omega_n < 1$ indicates movement toward the right (decreasing

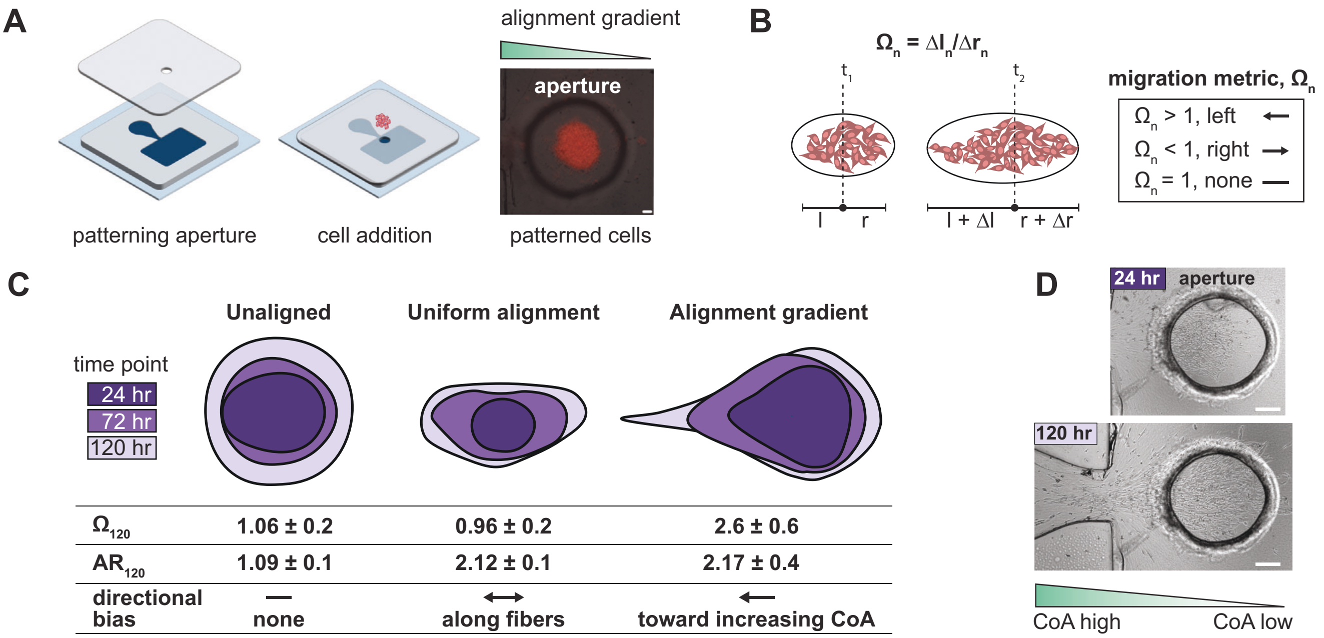

Figure 6. MDA-MB-231 cell patterning and biased migration on graded collagen gels. A) A schematic illustrating the process of patterning cell aggregates through the aperture with a representative image of fluorescently labeled cells patterned on a collagen gel. B) Cell movement was quantified by constructing an enclosed cell envelope that bounded the aggregate at each time point. The net movement of cells every 24 h was measured by calculating Ω_n, the ratio between the change in position of the left and right edges of the aggregate between successive time points. $\Omega_n > 1$ denotes net cell movement toward the left, $\Omega_n < 1$ toward the right, and $\Omega_n \approx 1$ represents equal cell movement left and right. C) The evolution of the enclosed cell envelopes (drawn to scale) at 24 (dark purple), 72 (purple), and 120 (light purple) h for unaligned, uniformly alignment, and graded alignment are shown. The aspect ratio (AR) is the ratio of the length to the width of the enclosed cell envelope. The $\Omega_{120} = 2.6 \pm 0.6$ for the gradient gel shows a clear tendency of cells to move toward increasing fiber alignment compared to unaligned ($\Omega_{120} = 1.06 \pm 0.2$) and uniformly aligned gels ($\Omega_{120} = 0.96 \pm 0.2$). The AR_{120} for the gradient gel compared to the unaligned gel shows the biased distribution of cells along the direction of alignment. The AR_{120} for aligned gel indicated a bi-directional spread while the AR_{120} for the unaligned gel indicated migration in all directions. D) Representative brightfield images of cells on gradient channels captured at 24 and 120 h from seeding with the fiber alignment increasing toward the left. Cells on the gradient channel after 120 h show preferential migration toward the left (increasing fiber alignment). Ω and AR are presented as mean ± SD, $n = 3$ independent experiments. Scale bar = 200 µm.

CoA), and $\Omega_n \approx 1$ indicates no preferential directionality. The length-to-width aspect ratio of the envelope (AR_n) was calculated at each time point to assess cell distribution , with larger values of AR_n indicating an increased spread along the fibers.

Gradient gel behavior was compared to corresponding responses using unaligned (CoA < 0.5) and uniformly aligned gels (CoA > 0.65). To visualize the migratory behavior, we present the evolution of the enclosed cell envelopes over the duration of the experiment (Figure 6C and Figure S11, Supporting Information). Cells on graded alignment exhibited $\Omega_{120} = 2.6 \pm 0.6$, which indicated a directionally biased migration toward increasing alignment. This was statistically larger ($p < 0.002$) than both the control conditions, where $\Omega_{120} \approx 1$ (unaligned $\Omega_{120} = 1.06 \pm 0.2$ and uniformly aligned $\Omega_{120} = 0.96 \pm 0.2$) (Figure S12, Supporting Information). The Ω_{120} values for both indicated no left-to-right biasing, but the enclosed cell envelopes appeared quite different. These differences were quantified using the aspect ratio AR_{120}. In the uniformly aligned condition, the aspect ratio of 2.12 ± 0.1 indicated bi-directional migration, with cells equally distributed along the axis of alignment. Conversely, in the unaligned conditions $AR_{120} = 1.09 \pm 0.1$ and represented random walk behavior with equal migration in all directions (Figure S12, Supporting Information). Figure 6D shows the bright field images of cells on the fiber alignment gradient 24 and 120 h after seeding.

The results presented here represent the first report of engineered fiber alignment gradients in soft biomaterials combined with a direct comparison of cell responses on graded and uniformly aligned architectures. Our data on single HUVEC and aggregated MDA-MB-231 responses provided evidence that the cells migrated more directionally on the subtly graded architecture and exhibited bi-directional migration on uniformly aligned gels. These findings were consistent with classical taxis cues where a spatially graded signal elicits a more potent response than a homogeneous presentation.[32,62]

Although contact guidance has been studied in several contexts, the mechanism that promotes directional migration in the absence of an intrinsic asymmetry in the signal (e.g., no preferred directionality along the aligned fibers) is not entirely understood. One explanation is based on the anisotropic mechanical resistance hypothesis that explored the migration of dermal fibroblasts in fibrin gels that contained uniform fiber alignment with constant adhesion strength and porosity.[77] Crosslinked and stiffened gels exhibited anisotropy in mechanical resistance along and perpendicular to the fiber direction that could be sensed by the cells. One possible explanation for the observed behavior on graded fibers is that filopodia probing the substrate in the direction of increasing alignment matured and grew more than those sampling lower alignment regions, thereby polarizing the cells in the direction of increasing alignment.[80,83] The open access design and cell patterning features of our platform can allow a more detailed understanding of the molecular underpinnings that drive differences in behavior between graded and uniform contact guidance cues.

An additional strength of our platform lies in the simplicity of the geometry-based biofabrication approach, which does not require specialized equipment. The microfluidic device can be made using a laser cutter and soft lithography techniques. The basic constricting and expanding channel design provides a straightforward and accessible approach to achieve controlled fiber alignment gradients. We anticipate this operationally simple design approach will allow other research laboratories to investigate the role of alignment gradients in contact guidance, with broad relevance to tumor invasion, angiogenesis, and immune trafficking.

One limitation of our platform is that the thickness of the microengineered gel is defined by the height of the flow channel (≈200 µm). With an increase in channel height, faster input flow rates are required to generate the extensional flow characteristics to create graded alignment. These faster flow rates can cause device failure near the constriction and serve as a practical limit on the achievable height of the engineered collagen gels. This issue can be addressed using our layer-by-layer fabrication technique that allows collagen layers to be added without disrupting the underlying structures[49] and allows multiple gel materials to be introduced.

3. Conclusion

This work introduces a simple geometry-based microfluidic approach toengineer tunable sub-millimeter to millimeter scale fiber alignment gradients within a 3D collagen-based material library for the first time. Our reversibly sealed channel design allows direct access to the microengineered gels and enables controlled cell patterning at defined locations, facilitating directed migration studies in graded fiber alignment landscapes. We provide new evidence that single HUVECs and patterned MDA-MB-231 aggregates respond to subtle gradients in fiber alignment with biased migration toward increasing fiber alignment. We anticipate that this first-of-its-kind biofabrication technique to engineer alignment gradients will enable new studies to explore how different cell populations interpret complex fiber architectures and shed new light on contact guidance cues.

4. Experimental Section

Banked Patient Samples and Second Harmonic Generation Imaging: This work imaged tumor-stroma interface in biopsy samples of triple-negative breast cancer (TNBC) patients with Second Harmonic Generation (SHG) imaging. These patients were identified from the pathology files at the University of Rochester Medical Center (URMC), spanning 2009–2020. The use of patient samples was approved by the Institutional Review Board at the University of Rochester (IRB RSRB00069270).

To image the collagen fibers in the TME, this work used a Spectra-physics MaiTai Ti:Sapphire laser directed through an Olympus Fluoview FV300 scanner and a BX61WI upright microscope. The laser's circular polarization was confirmed to ensure equal excitation of all fiber orientations. The laser was focused through an Olympus UMPLFL20XW water-immersion lens, which also collected the backward-scattered SHG signal. This signal was separated from the excitation beam, filtered, and detected by a photomultiplier tube. The forward scattered SHG signal was collected by an Olympus 0.9 NA condenser, reflected, filtered, and detected by another photomultiplier tube. We collected 512 × 512 pixel images as a Z-stack in 3 µm steps and then maximum-intensity projected to form a single forward-detected image. The fiber alignment in a forward detected image was assessed by dividing the image into 200 × 200 µm regions and calculating the coefficient of alignment (CoA) for each. CoA values can range from 0.25 to 1, representing low to high fiber alignment, with a value of 0.5 serving as the threshold for alignment.

Resealable Microchannel Fabrication: A mold was first created using standard soft lithography techniques.[20,49,84] Briefly, a negative photoresist, SU-8 3050 (Kayaku Advanced Materials, MA, USA), was spin-coated on a 100 mm diameter silicon wafer (University Wafers, MA, USA) to a thickness of 200 µm. The spin-coated height (200 µm) defined the height of the microchannel. The photoresist was then soft-baked at 95 °C for 60 min, followed by exposure to 365 nm UV (250 mJ cm^{-2}) through a high-resolution printed photomask. The wafer was baked at 95 °C for 5 min, cooled to room temperature, and immersed in a SU-8 developer solution to remove the non-crosslinked photoresist. The wafer was then rinsed with isopropanol and dried under pressurized air.

The PDMS base and crosslinker (Sylgard 184, Dow Corning, Midland USA) were mixed in a 10:1 ratio and degassed the mixture in a vacuum chamber for 30 min to remove bubbles. The degassed PDMS was poured on the silicone mold and created a stack consisting of a transparency sheet, a metal plate, and a 6 kg mass. The mass pushed excess PDMS away from the SU-8 features and created a through-cut channel geometry, with a height of the feature defined by the SU-8. The stack was cured at 80 °C for 1 h on a hotplate. After cooling to room temperature, the transparency sheet was carefully removed from the mold. The through-cut PDMS sheet was then peeled from the mold and inspected. The PDMS was cut into individual sections and cleaned with 70% ethanol solution and DI water. The through-cut PDMS sheet was treated with air plasma on one side and bonded to a glass coverslip to form a microchannel with 200 µm height. A PDMS lid with ports for injecting collagen was sealed against the PDMS channel footprint using conformal contact. This process results in the formation of a 3D collagen gel defined by the height of the channel. Here, channel height was 200 µm.

To fabricate PDMS lids, lid shapes were laser cut into 1.5 mm thick acrylic sheets and attached to a silicon wafer using pressure sensitive adhesive (PSA, 3M, MN, USA) film, yielding six square-shaped cavities, each having 20 mm sides and a 1.5 mm depth. Following this, the silicon mold was filled with degassed PDMS, allowing us to create lids of 1.5 mm thickness. The silicon mold was then heated at 80 °C for 1 h, allowing it to cool to room temperature. To finish, the lids were removed from the mold and cleaned using a 70% ethanol solution. The clean lids were then stored with protective tape applied to both faces.

Coverslip Functionalization and PDMS Passivation: To enhance the attachment of collagen to the coverslip, this work functionalized coverslips with poly(octadecene maleic alt-1-anhydride) (POMA) using established protocols.[20,85,86] Briefly, the coverslips were cleaned with 70% ethanol and dried under a pressurized air stream. The coverslips were then exposed to O_2 plasma for 1 min at 600 mTorr (Harrick Plasma, NY, USA) to activate their surface. Next, the coverslips were immersed in a 2% v/v solution of aminopropyltriethoxysilane (APTES) (Millipore Sigma, MA, USA) and placed on a rocker for 5 min. Following this step, the coverslips were rinsed with ethanol, dried under pressurized air, and baked on a hot plate for 10 min at 110 °C. The POMA solution was prepared by dissolving poly(octadecene maleic alt-1-anhydride) (Millipore Sigma, MA, USA) in 99.9% tetrahydrofuran (Millipore Sigma, MA, USA), and the coverslips were spin-coated with this solution. Finally, the POMA-coated coverslips were placed on a hot plate for 1 h at 120 °C.

To prevent the unwanted attachment of collagen to the PDMS lid, the surfaces were passivated by immersing them in 4% w/v Bovine Serum Albumin (BSA) in 1× PBS for 4 h at 4 °C. The PDMS lids were rinsed 3×

with phosphate buffered saline (PBS), air dried, and stored in a closed Petri dish until use.

Collection Solution Preparation and Injection: Atelo collagen: A total of 416 µL of bovine atelo Type I collagen solution (Neutragen, Advanced Biomatrix, CA, USA) was diluted with 429 µL of ultra-pure water, 55 µL of 0.1 M Sodium hydroxide (VWR, PA, USA), and 100 µL of 10X phosphate-buffered solution (ThermoFisher Scientific, MA, USA) to achieve a final collagen concentration of 2.5 mg mL^{-1}. The pH of the neutralized collagen solution was adjusted to 8.7–9.2 using 0.1 M NaOH and measured with a pH probe (A511 Orion Star, ThermoFisher, USA) after each preparation.

Methacrylated collagen: Photoactive methacrylated Type I Bovine Telo collagen kit was purchased from Advanced Biomatrix (Neutragen, Advanced Biomatrix, CA, USA). A 3 mg mL^{-1} collagen stock solution was mixed with the neutralizing solution and the photoinitiator Irgacure 2959 to achieved a final collagen concentration of 2.7 mg mL^{-1} following the recommended protocol, resulting in a pH between 7.4 and 7.6. After polymerizing the collagen mixture, we crosslinked the collagen hydrogel by exposing the device to 365 nm UV light at 10 mW cm^{-2} for 275 s.

A syringe pump (New Era Pump Systems, NY, USA) was used to inject neutralized collagen solution into PDMS microchannels in two phases. During the first phase, collagen was injected into port 1 at a flow rate of 500 nL min^{-1} using a 20-gauge dispensing needle (Grainger Industrial Supply, IL, USA) while all ports were open. Preloading the channel with collagen prevented air bubbles from forming during the next step. In the second phase, ports 2 and 4 were closed, and collagen was injected at varying flow rates ($Q = 10$, 100, and 500 µL min^{-1}) from port 1 to port 4. The injections were conducted at room temperature (21 °C). The chip was then incubated in a petri dish at 37 °C for 1 h to facilitate collagen polymerization. A damp Kim wipe (Kimtech, Kemberly-Clark Professional, TX, USA) was placed in the petri dish to prevent evaporation.

Microparticle Image Velocimetry: Microparticle image velocimetry (µPIV) to measure the velocity of the neutralized collagen solution. The measurements were performed using a Nikon Eclipse TE2000-S microscope equipped with a pulsed laser (TSI Incorporated, MN, USA). A mixture of 2.7 mg mL^{-1} of neutralized collagen solution and 5 µm fluorescent polystyrene latex particles (0.1% w/v) (Magsphere, CA, USA) were injected at $Q = 500$, 100, and 10 µL min^{-1} from the inlet of the microfluidic chip using a syringe pump. To obtain the PIV data, this work performed measurements on three independent samples in three different regions. This work analyzed ten pairs of images, captured at 10 µs intervals within a 700 × 700 µm region centered on the microchannels. The velocity of the neutralized collagen solution was calculated using TSI Insight 4G software (TSI, MN, USA).

Confocal Imaging and Analysis of Collagen Fibers: This work used a Leica SP5 laser scanning confocal microscope equipped with a 40× water immersion objective and 1.75× optical zoom to image collagen fibers. This work captured 2 µm image stacks consisting of 13 images at $z = 30$ µm from the coverslip. Collagen fibers were imaged in reflectance mode using a 488 nm laser. To analyze the images, the image slices were projected onto a single plane using the average projection feature in Fiji (NIH, USA) before analysis.

Olympus IX-81 microscope with a 4× objective was used for cell patterning imaging. This work used the Leica SP5 microscope with a 20× objective and an incubated stage with temperature and gas control to conduct the migration experiment. This work loaded the coverslips containing the gradient channels and patterned cells onto a 6-well plate and placed them on the microscope stage. The 6-well plate was incubated on the microscope stage for 1 h before starting imaging.

This work analyzed confocal reflectance microscopy images using LOCI CT-FIRE, a MATLAB-based code,[87] to measure fiber alignment. This work obtained a histogram of fiber angle distribution in 15° bins for each image and calculated the coefficient of alignment (CoA) as the ratio of the number of fibers within ±15° of the mode on the histogram to the total number of fibers. A CoA > 0.5 indicated aligned fibers, and CoA < 0.5 indicated unaligned fiber arrangement. These methods allowed us to accurately measure fiber alignment and assess cell migration in our experiments.

Pore Diameter, Fiber Density, and Cell Motility Characterization: To analyze the pore characteristics of our gels, this work employed a method previously described by Taufalele et al.[59] The initial step involved projecting an image stack onto a single plane. These images measured 221.64 × 221.64 microns in the x and y directions, with a pixel µm^{-1} ratio of 4.623. In this case, each z-stack consisted of 13 slices, which were projected onto a single plane using the average projection in Fiji. The projection was imported to MATLAB, the Erode Cutoff was set to one, and a top-hat filter was applied to adjust contrast. The projected image was binarized to determine the fiber fraction, and a ratio of bright pixels to total pixels was calculated and reported as the fiber fraction for each group of images corresponding to the high, medium, and low CoA categories.

To track the migration of the cell front, the 2024 × 2024 cell aggregate microscope image was first cropped to a 1734 × 1024 image that included the cell-containing region, using Fiji. All images were then aligned using a translating function so that the center point of the patterning aperture coincided across all images. To align images in the aligned and unaligned controls channel feature across the images was used as reference. Next, a grid was established across the aligned images to measure the cell distance to the left and right. To identify the cells within the image, a 3 × 3 second derivative convolution filter was applied, which helped subtract the patterning aperture from the image. Next, a variance filter with a 2-pixel radius was used to enhance the contrast between cells and their surroundings, improving the tracking of the cell front. Finally, the resultant image was converted into a binary black and white frame (enclosed area) using the Fiji Otsu threshold filter, allowing us to calculate the distance of both cell fronts from the previously marked center point.

Nanoindentation: As described previously,[49] collagen was injected into step channels, allowed to polymerize, and then exposed to UV to crosslink the gel. Confocal imaging was then used to characterize CoA. To measure the local stiffness, a nanointentor (Optics11 Piuma) with a 27 µm spherical probe was used to collect force displacement curves fit to the Hertz contact model using 20 points over a 2 mm matrix scan, with a reading every 100 µm in aligned (CoA $= 0.6 \pm 0.02$) and unaligned (CoA $= 0.4 \pm 0.02$) gels ($n = 3$). The average values from 20 data points in three independent gels (aligned and unaligned) were used to compare values.

Cell Culture and Cell Aggregate Formation: MDA-MB-231 cells (ATCC, VA, USA) were cultured in DMEM (Gibco, ThermoFisher, MA, USA) supplemented with 10% Fetal Bovine Serum (FBS). Human Umbilical Vein Endothelial Cells (HUVECs) (ATCC, VA, USA) were cultured in Endothelial Cell Basal Medium (EBM) supplemented with the Endothelial Growth Media kit (EGM-2) (CC-3162, Lonza, Basel, Switzerland). All cells were maintained at 37 °C and 5% CO2 and used between passage number 3–7. The suspended cells after passaging were mixed with methylcellulose to get a final concentration of 20% methylcellulose (M0512, Sigma Aldrich, MO, USA) in the media by volume. Loose MDA-MB-231 cell aggregates were formed using a hanging drop method by adding 2000 cells per drop into an untreated 1-well plate and incubated at 37 °C for 2 days. The resulting cell aggregates were then labeled with CMRA cell tracker dye (ThermoFisher, MA, USA) or unlabeled.

Cell Tracking and Analysis: 40 cells for the unaligned collagen and 20 cells each for aligned and gradient conditions were manually tracked using TrackMate in Fiji to generate x and y coordinates for each cell for all frames. In the uniformly aligned region (Figure 5B), although the fibers are aligned, they are at a 30° angle due to the constriction. To account for this, the frames were rotated 30° in the anti-clockwise direction to make the fiber alignment direction consistent (same fiber alignment direction as the gradient). Next, the directional migration of cells on the three conditions was assessed by the Chemotaxis and Migration Tool (Ibidi, BY, Germany). The Forward migration index (FMI) parallel and perpendicular to the alignment direction, along with the velocity of the individual cell, was calculated (Figure S10, Supporting Information). For the unaligned condition, there is no principal axis that is perpendicular or parallel for migration. For consistency of notation with the other two conditions, the y-axis is the direction for parallel migration and the x-axis as the migration direction perpendicular to alignment. As shown in Figure S10, Supporting Information, there is no difference in FMI for cells on the unaligned condition between the two axes. Next, this work tracked the time for which the cell continued to travel in a particular direction before changing by persistent random walk model, as shown by Wu and coworkers.[81,82] This model allowed the calculation of the persistence time for individual cells based on their tracked x and y coordinates by fitting the position and time point data of individual cells to the persistent random walkmodel.

Cell Patterning: After collagen gel formation, the functionalized PDMS lids were carefully peeled away, and 500 µL of media was added to the collagen gel, which was then placed in an incubator overnight. Following incubation, the excess liquid was removed from the collagen surface, and a 200 µm thick PDMS sheet containing a laser cut 500 µm diameter patterning aperture was positioned on the collagen, providing direct access to a defined region of the gel.

To pattern a cell aggregate, the aggregate was removed from a non-treated U-shaped bottom plate using a sterile spatula and added to the patterning aperture, settling on the collagen gel within the aperture footprint.

Cell Labeling and Immunostaining: CMRA cell tracker dye (ThermoFisher Scientific, MA, USA) was diluted to a concentration of 25 µM in cell media and added to the culture flask to enable live tracking of cells. The cells were incubated with the dye for 30 min, followed by replacing the media containing the CMRA stain with a culture medium.

For immunostaining, the cells were fixed with 4% paraformaldehyde (ThermoFisher Scientific, MA, USA) and permeabilized with 0.1% Triton X-100 (J63521, Alfa Aesar, MA, USA) for 15 min. The permeabilized cells were then blocked with 4% Bovine Serum Albumin (BSA) (VWR, PA, USA) for 30 min, and each step was followed by washing the cells with PBS Tween 20 (ThermoFisher Scientific, MA, USA).

Statistical Analysis: In multi-comparison analysis, this work assessed normality using the Shapiro-Wilk test ($n < 50$). We selected the appropriate test for multiple comparisons depending on whether the data was normally distributed and if variances were equal. Standard one-way ANOVA was used for normally distributed; non-parametric Kruskal-Wallis for non-normal distributions; and Brown-Forsythe/Welch's ANOVA for data with unequal variances. Post hoc tests were used to determine differences between sample groups. For direct comparisons between two groups, we chose a parametric or a non-parametric t-test, based on the normality results from the Shapiro-Wilk test. A p-value less than 0.05 was considered statistically significant. All statistical analyses were performed using GraphPad Prism 9.0 software (GraphPad Software, CA, USA). ns = not significant, $^*p < 0.05$, $^{**}p < 0.002$, $^{***}p < 0.0002$, and $^{****}p < 0.0001$.

Supporting Information

Supporting Information is available from the Wiley Online Library or from the author.

Acknowledgements

The authors acknowledge Prof. Thomas Gaborski for assistance with cell motility analysis, Prof. Steven Day for µPIV measurements, Vincent Mei and Prof. Christopher Lewis for assistance with rheometry and UV exposure studies. The authors also thank Meng-Chun Hsu, Ann Byerley, Madeleine Goulet, Aidan Hughes, Lauren Audi, and Anna Carter of the Biological Microsystems Laboratory at RIT for insightful discussions. VVA dedicates this work to the memory of LG Abhyankar (1925-2023). This work was partially supported by the NIH under grant numbers R21GM143658, R16GM146687, and NSF grants CBET 2150798 and 215099. This content is solely the responsibility of the authors and does not necessarily represent the official views of the National Institutes of Health or the National Science Foundation. [Correction added on 17 January 2024, after first online publication: figure 4A, low CoA group data points.]

Conflict of Interest

The authors declare no conflict of interest.

Data Availability Statement

The data that support the findings of this study are available from the corresponding author upon reasonable request.

Keywords

biofabrication, collagen fiber alignment, contact guidance, directional cell migration, microfluidics

Received: July 13, 2023
Revised: November 6, 2023
Published online: December 17, 2023

---

[1] D. Stopak, A. K. Harris, *Dev. Biol.* **1982**, *90*, 383.
[2] H. Wang, A. S. Abhilash, C.-S. Chen, R.-G. Wells, V.-B. Shenoy, *Biophys. J.* **2015**, *107*, 2592.
[3] J. Sapudom, S. Karaman, B. C. Quartey, W. K. E. Mohamed, N. Mahtani, A. Garcia-Sabaté, J. Teo, *Adv. Sci.* **2023**, *10*, 2301353.
[4] J. H. Ahrens, S. G. M. Uzel, M. Skylar-Scott, M. M. Mata, A. Lu, K. T. Kroll, J. A. Lewis, *Adv. Mater.* **2022**, *34*, 2200217.
[5] L. D. Black, J. D. Meyers, J. S. Weinbaum, Y. A. Shvelidze, R. T. Tranquillo, *Tissue Eng., Part A* **2009**, *15*, 3099.
[6] A. Agrawal, B. H. Lee, S. A. Irvine, J. An, R. Bhuthalingam, V. Singh, K. Y. Low, C. K. Chua, S. S. Venkatraman, *Int. J. Biomater.* **2015**, *2015*, 1.
[7] M. W. Conklin, J. C. Eickhoff, K. M. Riching, C. A. Pehlke, K. W. Eliceiri, P. P. Provenzano, A. Friedl, P. J. Keely, **2011**, *178*, 12.
[8] C. R. Drifka, A. G. Loeffler, K. Mathewson, A. Keikhosravi, J. C. Eickhoff, Y. Liu, S. M. Weber, W. J. Kao, K. W. Eliceiri, *OncoTargets Ther.* **2016**, *7*, 76197.
[9] A. L. Bauer, T. L. Jackson, Y. Jiang, *PLoS Comput. Biol.* **2009**, *5*, 1000445.
[10] J.-H. Lee, P. Parthiban, G.-Z. Jin, J. C. Knowles, H.-W. Kim, *Prog. Mater. Sci.* **2021**, *117*, 100732.
[11] H. C. Pruitt, D. Lewis, M. Ciccaglione, S. Connor, Q. Smith, J. W. Hickey, J. P. Schneck, S. Gerecht, *Matrix Biol.* **2020**, *85*, 147.
[12] S. Alkmin, R. Brodziski, H. Simon, D. Hinton, R. H. Goldsmith, M. Patankar, P. J. Campagnola, *Cancers (Basel)* **2020**, *12*, 1390.
[13] P. P. Provenzano, K. W. Eliceiri, J. M. Campbell, D. R. Inman, J. G. White, P. J. Keely, *BMC Med.* **2006**, *4*, 38.
[14] A. Ray, R. K. Morford, N. Ghaderi, D. J. Odde, P. P. Provenzano, *Integr. Biol.* **2018**, *10*, 100.
[15] B. A. Nerger, P.-T. Brun, C. M. Nelson, *Soft Matter* **2019**, *15*, 5728.
[16] A. Mazzocchi, M. Devarasetty, R. Huntwork, S. Soker, A. Skardal, *Biofabrication* **2018**, *11*, 015003.
[17] Z. Wu, B. Kong, R. Liu, W. Sun, S. Mi, *Nanomaterials* **2018**, *8*, 124.
[18] S. Zhong, W. E. Teo, X. Zhu, R. W. Beuerman, S. Ramakrishna, L. Y. L. Yung, *J. Biomed. Mater. Res., Part A* **2006**, *79A*, 456.
[19] C. Guo, L. J. Kaufman, *Biomaterials* **2007**, *28*, 1105.
[20] A. Ahmed, I. M. Joshi, S. Larson, M. Mansouri, S. Gholizadeh, Z. Allahyari, F. Forouzandeh, D. A. Borkholder, T. R. Gaborski, V. V. Abhyankar, *Adv. Mater. Technol.* **2021**, *6*, 2001186.
[21] D. Vader, A. Kabla, D. Weitz, L. Mahadevan, *PLoS One* **2009**, *4*, 5902.
[22] B. A. Nerger, P.-T. Brun, C. M. Nelson, *Sci. Adv.* **2020**, *6*, eaaz7748.
[23] A. Ahmed, I. M. Joshi, M. Mansouri, N. N. N. Ahamed, M.-C. Hsu, T. R. Gaborski, V. V. Abhyankar, *Am. J. Physiol.: Cell Physiol.* **2021**, *320*, C1112.
[24] P. Pakshir, M. Alizadehgiashi, B. Wong, N. M. Coelho, X. Chen, Z. Gong, V. B. Shenoy, C. A. Mcculloch, B. Hinz, *Nat. Commun.* **2019**, *10*, 1850.

[25] W.-H. Jung, N. Yam, C.-C. Chen, K. Elawad, B. Hu, Y. Chen, *Biomaterials* **2020**, *234*, 119756.
[26] M. Musiime, J. Chang, U. Hansen, K. E. Kadler, C. Zeltz, D. Gullberg, *Cells* **2021**, *10*, 662.
[27] B. J. Duchez, A. D. Doyle, E. K. Dimitriadis, K. M. Yamada, *Biophys. J.* **2019**, *116*, 670.
[28] A. Shellard, R. Mayor, *Nature* **2021**, *600*, 690.
[29] J. Renkawitz, A. Kopf, J. Stopp, I. D. Vries, M. K. Driscoll, J. Merrin, R. Hauschild, E. S. Welf, G. Danuser, R. Fiolka, M. Sixt, *Nature* **2019**, *568*, 546.
[30] A. J. Lomakin, C. J. Cattin, D. Cuvelier, Z. Alraies, M. Molina, G. P. F. Nader, N. Srivastava, P. J. Sáez, J. M. Garcia-Arcos, I. Y. Zhitnyak, A. Bhargava, M. K. Driscoll, E. S. Welf, R. Fiolka, R. J. Petrie, N. S. De Silva, J. M. González-Granado, N. Manel, A. M. Lennon-Duménil, D. J. Müller, M. Piel, *Science* **2020**, *370*, eaba2894.
[31] M. J. Oudin, O. Jonas, T. Kosciuk, L. C. Broye, B. C. Guido, J. Wyckoff, D. Riquelme, J. M. Lamar, S. B. Asokan, C. Whittaker, D. Ma, R. Langer, M. J. Cima, K. B. Wisinski, R. O. Hynes, D. A. Lauffenburger, P. J. Keely, J. E. Bear, F. B. Gertler, *Cancer Discov.* **2016**, *6*, 516.
[32] S. Sengupta, C. A. Parent, J. E. Bear, *Nat. Rev. Mol. Cell Biol.* **2021**, *22*, 529.
[33] C. M. Morrow, A. Mukherjee, M. A. Traore, E. J. Leaman, A. Kim, E. M. Smith, A. S. Nain, B. Behkam, *Lab Chip* **2019**, *19*, 3641.
[34] C. Janetopoulos, R. A. Firtel, *FEBS Lett.* **2008**, *582*, 2075.
[35] H. E. Balcioglu, B. Van De Water, E. H. J. Danen, *Sci. Rep.* **2016**, *6*, 22580.
[36] A. Ray, Z. M. Slama, R. K. Morford, S. A. Madden, P. P. Provenzano, *Biophys. J.* **2017**, *112*, 1023.
[37] R. B. Dickinson, S. Guido, R. T. Tranquillo, *Ann. Biomed. Eng.* **1994**, *22*, 342.
[38] K. E. Kubow, V. D. Shuklis, D. J. Sales, A. R. Horwitz, *Sci. Rep.* **2017**, *7*, 14380.
[39] M. Antman-Passig, S. Levy, C. Gartenberg, H. Schori, O. Shefi, *Tissue Eng. Part A* **2017**, *23*, 403.
[40] J. M. Szulczewski, D. R. Inman, M. Proestaki, J. Notbohm, B. M. Burkel, S. M. Ponik, *Acta Biomater.* **2021**, *129*, 96.
[41] C. D. Lawson, A. J. Ridley, *J. Cell Biol.* **2017**, *217*, 447.
[42] J. H. R. Hetmanski, H. De Belly, I. Busnelli, T. Waring, R. V. Nair, V. Sokleva, O. Dobre, A. Cameron, N. Gauthier, C. Lamaze, J. Swift, A. Del Campo, T. Starborg, T. Zech, J. G. Goetz, E. K. Paluch, J.-M. Schwartz, P. T. Caswell, *Dev. Cell* **2019**, *51*, 460.
[43] S. J. King, S. B. Asokan, E. M. Haynes, S. P. Zimmerman, J. D. Rotty, J. G. Alb Jr, A. Tagliatela, D. R. Blake, I. P. Lebedeva, D. Marston, H. E. Johnson, M. Parsons, N. E. Sharpless, B. Kuhlman, J. M. Haugh, J. E. Bear, *J. Cell Sci.* **2016**, *129*, 2329.
[44] V. V. Abhyankar, M. W. Toepke, C. L. Cortesio, M. A. Lokuta, A. Huttenlocher, D. J. Beebe, *Lab Chip* **2008**, *8*, 1507.
[45] E. Inyang, V. Abhyankar, B. Chen, M. Cho, *Sci. Rep.* **2020**, *10*, 3054.
[46] A. P. Kishan, A. B. Robbins, S. F. Mohiuddin, M. Jiang, M. R. Moreno, E. M. Cosgriff-Hernandez, *Acta Biomater.* **2017**, *56*, 118.
[47] G. Z. Tan, Y. Zhou, *Nano-Micro Lett.* **2018**, *10*, 73.
[48] H. G. Sundararaghavan, J. A. Burdick, *Biomacromolecules* **2011**, *12*, 2344.
[49] A. Ahmed, M. Mansouri, I. M. Joshi, A. M. Byerley, S. W. Day, T. R. Gaborski, V. V. Abhyankar, *Biofabrication* **2022**, *14*, 035019.
[50] S. Köster, J. B. Leach, B. Struth, T. Pfohl, J. Y. Wong, *Langmuir* **2007**, *23*, 357.
[51] J. A. Paten, S. M. Siadat, M. E. Susilo, E. N. Ismail, J. L. Stoner, J. P. Rothstein, J. W. Ruberti, *ACS Nano* **2016**, *10*, 5027.
[52] B. P. Heller, D. E. Smith, D. A. Jack, *Addit. Manuf.* **2016**, *12*, 252.
[53] M. A. G. Cunha, M. O. Robbins, *Macromolecules* **2020**, *53*, 8417.
[54] N. Saeidi, E. A. Sander, J. W. Ruberti, *Biomaterials* **2009**, *30*, 6581.
[55] E. K. Hobbie, H. Wang, H. Kim, S. Lin-Gibson, E. A. Grulke, *Phys. Fluids* **2003**, *15*, 1196.
[56] F. Del Giudice, S. J. Haward, A. Q. Shen, *J. Rheol.* **2017**, *61*, 327.
[57] J. Dinic, Y. Zhang, L. N. Jimenez, V. Sharma, *ACS Macro Lett.* **2015**, *4*, 804.
[58] X. Gong, J. Kulwatno, K. L. Mills, *Acta Biomater.* **2020**.
[59] P. V. Taufalele, J. A. Vanderburgh, A. Muñoz, M. R. Zanotelli, C. A. Reinhart-King, *PLoS One* **2019**, *14*, 0216537.
[60] K. E. Sung, G. Su, C. Pehlke, S. M. Trier, K. W. Eliceiri, P. J. Keely, A. Friedl, D. J. Beebe, *Biomaterials* **2009**, *30*, 4833.
[61] L. Lara Rodriguez, I. C. Schneider, *Integr. Biol.* **2013**, *5*, 1306.
[62] A. Shellard, R. Mayor, *Trends Cell Biol.* **2020**, *30*, 852.
[63] J. Wondergem, M. Mytiliniou, F. Wit, T. Reuvers, D. Holcman, D. Heinrich, **2019**.
[64] J. Sapudom, S. Rubner, S. Martin, T. Pompe, *Adv. Healthcare Mater.* **2016**, *5*, 1861.
[65] F. Bordeleau, L. N. Tang, C. A. Reinhart-King, *Phys. Biol.* **2013**, *10*, 065004.
[66] E. George, I. Jahan, A. Barai, V. Ganesan, S. Sen, *Biomed. Mater.* **2021**, *16*, 054103.
[67] A. J. Berger, K. M. Linsmeier, P. K. Kreeger, K. S. Masters, *Biomaterials* **2017**, *141*, 125.
[68] B. R. Seo, X. Chen, L. Ling, Y. H. Song, A. A. Shimpi, S. Choi, J. Gonzalez, J. Sapudom, K. Wang, R. C. Andresen Eguiluz, D. Gourdon, V. B. Shenoy, C. Fischbach, *Proc. Natl. Acad. Sci. USA* **2020**, *117*, 11387.
[69] R. B. Martin, J. Ishida, *J. Biomech.* **1989**, *22*, 419.
[70] V. V. Abhyankar, M. Wu, C.-Y. Koh, A. V. Hatch, *PLoS One* **2016**, *11*, 0156341.
[71] M. Mansouri, A. Ahmed, S. D. Ahmad, M. C. Mccloskey, I. M. Joshi, T. R. Gaborski, R. E. Waugh, J. L. Mcgrath, S. W. Day, V. V. Abhyankar, *Adv. Healthcare Mater.* **2022**, 2200802.
[72] M.-C. Hsu, M. Mansouri, N. N. N. Ahamed, S. M. Larson, I. M. Joshi, A. Ahmed, D. A. Borkholder, V. V. Abhyankar, *Sci. Rep.* **2022**, *12*, 10769.
[73] S. G. M. Uzel, R. J. Platt, V. Subramanian, T. M. Pearl, C. J. Rowlands, V. Chan, L. A. Boyer, P. T. C. So, R. D. Kamm, *Sci. Adv.* **2016**, *2*, 1501429.
[74] S. Han, K. Yang, Y. Shin, J. S. Lee, R. D. Kamm, S. Chung, S.-W. Cho, *Lab Chip* **2012**, *12*, 2305.
[75] W. Han, S. Chen, W. Yuan, Q. Fan, J. Tian, X. Wang, L. Chen, X. Zhang, W. Wei, R. Liu, J. Qu, Y. Jiao, R. H. Austin, L. Liu, *Proc. Natl. Acad. Sci. USA* **2016**, *113*, 11208.
[76] A. Boussommier-Calleja, Y. Atiyas, K. Haase, M. Headley, C. Lewis, R. D. Kamm, *Biomaterials* **2019**, *198*, 180.
[77] B. Hagmeyer, F. Zechnall, M. Stelzle, *Biomicrofluidics* **2014**, *8*, 056501.
[78] M. J. Williams, N. K. Lee, J. A. Mylott, N. Mazzola, A. Ahmed, V. V. Abhyankar, *Micromachines* **2019**, *10*, 360.
[79] F. Baschieri, A. Illand, J. Barbazan, O. Zajac, C. Henon, D. Loew, F. Dingli, D. M. Vignjevic, S. Lévêque-Fort, G. Montagnac, *Sci. Adv.* **2023**, *9*, eade2120.
[80] K.-M. Riching, B. L. Cox, M.-R. Salick, C. Pehlke, A.-S. Riching, S. M. Ponik, B.-R. Bass, W.-C. Crone, Y. Jiang, A. M. Weaver, K.-W. Eliceiri, P.-J. Keely, *Biophys. J.* **2014**, *107*, 2546.
[81] P.-H. Wu, A. Giri, S. X. Sun, D. Wirtz, *Proc. Natl. Acad, Sci.* **2014**, *111*, 3949.

[82] P.-H. Wu, A. Giri, D. Wirtz, *Nat. Protoc.* **2015**, *10*, 517.

[83] G. R. Ramirez-San Juan, P. W. Oakes, M. L. Gardel, *Mol. Biol. Cell* **2017**, *28*, 1043.

[84] M. R. Hasan, S. S. S. Peri, V. P. Sabane, N. Mansur, J. X. Gao, K. T. Nguyen, J. A. Weidanz, S. M. Iqbal, V. V. Abhyankar, *Biomed. Phys. Eng. Express* **2018**, *4*, 025015.

[85] T. Pompe, S. Zschoche, N. Herold, K. Salchert, M.-F. Gouzy, C. Sperling, C. Werner*, *Maleic Anhydride Copolymers: A Versatile Platform for Molecular Biosurface Engineering*, American Chemical Society, Washington **2003**.

[86] T. Pompe, L. Renner, M. Grimmer, N. Herold, C. Werner, *Macromol. Biosci.* **2005**, *5*, 890.

[87] J. S. Bredfeldt, Y. Liu, C. A. Pehlke, M. W. Conklin, J. M. Szulczewski, D. R. Inman, P. J. Keely, R. D. Nowak, T. R. Mackie, K. W. Eliceiri, *J. Biomed. Opt.* **2014**, *19*, 016007.